β-decay properties of neutron-rich Ge, Se, Kr, Sr, Ru, and Pd isotopes from deformed quasiparticle random-phase approximation

P. Sarriguren*
Instituto de Estructura de la Materia, IEM-CSIC, Serrano 123, E-28006 Madrid, Spain
(Received 24 July 2014; revised manuscript received 5 February 2015; published 7 April 2015)

β-decay properties of even- and odd-A neutron-rich Ge, Se, Kr, Sr, Ru, and Pd isotopes involved in the astrophysical rapid neutron capture process are studied within a deformed proton-neutron quasiparticle random-phase approximation. The underlying mean field is described self-consistently from deformed Skyrme-Hartree-Fock calculations with pairing correlations. Residual interactions in the particle-hole and particle-particle channels are also included in the formalism. The isotopic evolution of the various nuclear equilibrium shapes and the corresponding charge radii are investigated in all the isotopic chains. The energy distributions of the Gamow-Teller strength as well as the β-decay half-lives are discussed and compared with the available experimental information. It is shown that nuclear deformation plays a significant role in the description of the decay properties in this mass region. Reliable predictions of the strength distributions are essential to evaluate decay rates in astrophysical scenarios.

DOI: 10.1103/PhysRevC.91.044304 PACS number(s): 21.60.Jz, 23.40.Hc, 27.60.+j, 26.30.−k

I. INTRODUCTION

The rapid structural changes occurring in the ground state and low-lying collective excited states of neutron-rich nuclei in the mass region $A = 80$–128 have been extensively studied both theoretically and experimentally (see, e.g., [1,2] and references therein). From the theoretical side, the equilibrium nuclear shapes in this mass region have been shown to suffer rapid changes as a function of the number of nucleons with competing spherical, axially symmetric prolate and oblate, and triaxial shapes at close energies. Both relativistic [3,4] and nonrelativistic [5–9] approaches agree in the general description of the nuclear structural evolution in this mass region, which is supported experimentally by spectroscopic studies [10–12], 2^+ lifetime measurements [13–15], and quadrupole moments for rotational bands [15], as well as by laser spectroscopy measurements [16].

However, the nuclear structure richness is not the only attractive feature characterizing these nuclei. Another remarkable property of nuclei in this mass region is that they are involved in the astrophysical rapid neutron capture process (r process), which is considered to be one of the main nucleosynthesis mechanisms leading to the production of heavy neutron-rich nuclei in the universe [17,18]. The r-process nucleosynthesis involves many neutron-rich unstable isotopes, whose neutron capture rates, masses, and β-decay half-lives ($T_{1/2}$) are crucial quantities to understand the possible r-process paths, the isotopic abundances, and the time scales of the process [18–20]. Although much progress was made measuring masses (see, for example, the Jyväskylä mass database [21]) and half-lives [22–24], most of the nuclear properties of relevance for the r process are experimentally unknown because of their extremely low production yields in the laboratory. Therefore, reliable nuclear physics models are required to simulate properly the r process.

The quasiparticle random-phase approximation (QRPA) is considered a well-suited model to describe medium-mass open-shell nuclear properties and specifically β-decay properties. QRPA calculations for neutron-rich nuclei have been carried out within different spherical formalisms, such as Hartree-Fock-Bogoliubov (HFB) [25], continuum QRPA with density functionals [26], and relativistic mean field approaches [27]. However, the mass region we are dealing with requires nuclear deformation as a relevant degree of freedom to characterize the nuclear structure involved in the calculation of the β-strength functions. The deformed QRPA formalism was developed in Refs. [28–31], using phenomenological mean fields. A Tamm-Dancoff approximation with Sk3 interaction was also implemented in Ref. [32]. More recently, deformed QRPA calculations using deformed Woods-Saxon potentials and realistic CD-Bonn residual forces have been performed in [33,34]. First-forbidden transitions were also considered in those references, showing that their effect in this mass region can be neglected. Various self-consistent deformed QRPA calculations to describe the β-decay properties, either with Skyrme [35] or Gogny [36] interactions are also available in the literature.

In Refs. [37,38] the decay properties of neutron-rich Zr and Mo isotopes were studied within a deformed proton-neutron QRPA based on a self-consistent Hartree-Fock (HF) mean field formalism with Skyrme interactions and pairing correlations in BCS approximation. Residual spin-isospin interactions were also included in the particle-hole and particle-particle channels [39,40]. In this work this study is extended to the neighboring regions including even and odd-A neutron-rich Ge, Se, Kr, Sr, Ru, and Pd isotopes. These calculations are timely because they address a mass region which is at the borderline of present experimental capabilities for measuring half-lives at MSU and RIKEN [22–24]. In addition, theoretical calculations can be tested with the available experimental information on half-lives providing simultaneously predictions for the underlying Gamow-Teller strength distributions and for the half-lives of more exotic nuclei not yet measured.

*p.sarriguren@csic.es

Finally, this more comprehensive study allows one to judge better the extent to which the method is able to describe the decay properties of nuclei in a wider mass region that includes spherical, well-deformed, and weakly deformed transitional isotopes, as well as isotopes exhibiting shape coexistence. Therefore, the theoretical method will be tested over a rich set of different nuclear structures that will reveal the limitations of the model.

The paper is organized as follows. In Sec. II a review of the theoretical formalism used is introduced. Section III contains the results obtained for the potential energy curves (PEC), Gamow-Teller (GT) strength distributions, and β-decay half-lives, which are compared with the experimental data. Section IV summarizes the main conclusions.

II. THEORETICAL FORMALISM

A summary of the theoretical framework used in this paper to describe the β-decay properties in neutron-rich isotopes is shown in this section. More details of the formalism can be found elsewhere [39,40]. The method starts from a self-consistent calculation of the mean field by means of a deformed Skyrme-Hartree-Fock procedure with pairing correlations in BCS approximation. Single-particle energies, wave functions, and occupation amplitudes are generated from this mean field. The Skyrme interaction SLy4 [41] is used as a representative of modern Skyrme forces. It was very successful describing nuclear properties all along the nuclear chart and was extensively studied [6,7,42].

The solution of the HF equation, assuming time reversal and axial symmetry, is found by using the formalism developed in Ref. [43]. The single-particle wave functions are expanded in terms of the eigenstates of an axially symmetric harmonic oscillator in cylindrical coordinates, using 12 major shells. The pairing gap parameters for protons and neutrons in the BCS approximation are determined phenomenologically from the odd-even mass differences [44]. In a further step, constrained HF calculations with a quadratic constraint are performed to construct the PECs, analyzing the nuclear binding energies in terms of the quadrupole deformation parameter β. Calculations for GT strengths are performed subsequently for the various minima in the energy curves indicating the equilibrium shapes of each nucleus. Because decays connecting different shapes are disfavored, similar shapes are assumed for the ground state of the parent nucleus and for all populated states in the daughter nucleus. The validity of this assumption was discussed for example in Refs. [28,30].

To describe GT transitions, a separable spin-isospin residual interaction in the particle-hole (ph) and particle-particle (pp) channels is added to the mean field and treated in a deformed proton-neutron QRPA [28–32,39,40,45]. An optimum set of coupling strengths could be chosen following a case-by-case fitting procedure and one will finally get different answers depending on the nucleus, shape, and Skyrme force. However, because the purpose here is to test the ability of QRPA to account for the GT strength distributions in this mass region with as few free parameters as possible, the same coupling strengths are used for all the nuclei considered in this paper, which are taken from previous works [37,38]. We use $\chi_{\rm GT}^{\rm ph} = 0.15$ MeV and $\kappa_{\rm GT}^{\rm pp} = 0.03$ MeV for the residual interaction in the ph and pp channels, respectively.

The sensitivity of the GT strength distributions to the various ingredients contributing to the deformed QRPA calculations, namely to the nucleon-nucleon effective force, to deformation, to pairing correlations, and to residual interactions, have been investigated in the past [39,40,46–48]. In this work the most reasonable choices found in those references are used. Summarizing the various sensitivities, the conclusion is that the main features of the GT strength distributions are in general very robust against the Skyrme force used, showing some more sensitivity in the spherical cases, where the location of the single-particle energies is more critical to determine the excitation energies of the GT transitions. Deformation was shown to be an important issue to describe the profiles of the GT strength distributions. First, because the degeneracy of the spherical shells is broken making the GT strength distributions more fragmented than the corresponding spherical ones. Secondly, because the energy levels of deformed orbitals cross each other in a way that depends on the magnitude of the quadrupole deformation as well as on the oblate or prolate character. This level crossing may lead in some instances to sizable differences in the GT profiles, a fact that was exploited to learn about the nuclear shape from the measured β-decay pattern [49–51]. Pairing correlations are also important to describe nuclei out of closed shells. Their influence on the GT profiles was studied in Ref. [40], concluding that the main effect is to decrease slightly the strength at low energies and to create new transitions, mainly at high energies, that are forbidden in the absence of such correlations. The effect of the ph and pp residual interactions is also well known. The repulsive ph interaction redistributes the GT strength by shifting it to higher excitation energies causing a displacement of the GT resonance. It also reduces somewhat the total strength. The attractive pp interaction moves the strength to lower energies. Its effect on the GT resonance is in general negligible, but nevertheless, the changes induced in the low-energy region are of great relevance in the calculation of the β-decay half-lives, which are only sensitive to the strength contained in the energy region below the Q-energy window.

The GT transition amplitudes in the intrinsic frame connecting the ground state $|0^+\rangle$ of an even-even nucleus to one-phonon states in the daughter nucleus $|\omega_K\rangle$ $(K = 0,1)$ are found to be

$$\langle \omega_K | \sigma_K t^{\pm} | 0 \rangle = \mp M_{\pm}^{\omega_K}, \tag{1}$$

where

$$M_{-}^{\omega_K} = \sum_{\pi\nu} \left(q_{\pi\nu} X_{\pi\nu}^{\omega_K} + \tilde{q}_{\pi\nu} Y_{\pi\nu}^{\omega_K} \right), \tag{2}$$

$$M_{+}^{\omega_K} = \sum_{\pi\nu} \left(\tilde{q}_{\pi\nu} X_{\pi\nu}^{\omega_K} + q_{\pi\nu} Y_{\pi\nu}^{\omega_K} \right), \tag{3}$$

with

$$\tilde{q}_{\pi\nu} = u_\nu v_\pi \Sigma_K^{\nu\pi}, \quad q_{\pi\nu} = v_\nu u_\pi \Sigma_K^{\nu\pi}, \tag{4}$$

in terms of the occupation amplitudes for neutrons and protons $v_{\nu,\pi} (u_{\nu,\pi}^2 = 1 - v_{\nu,\pi}^2)$ and the matrix elements of the spin

operator, $\Sigma_K^{\nu\pi} = \langle \nu | \sigma_K | \pi \rangle$, connecting proton and neutron single-particle states, as they come out from the HF + BCS calculation. $X_{\pi\nu}^{\omega_K}$ and $Y_{\pi\nu}^{\omega_K}$ are the forward and backward amplitudes of the QRPA phonon operator, respectively.

Once the intrinsic amplitudes in Eq. (1) are calculated, the GT strength $B_\omega(\mathrm{GT}^\pm)$ in the laboratory system for a transition $I_i K_i(0^+0) \rightarrow I_f K_f(1^+K)$ can be obtained as

$$B_\omega(\mathrm{GT}^\pm) = \sum_{\omega_K} [\langle \omega_{K=0} | \sigma_0 t^\pm | 0 \rangle^2 \delta(\omega_{K=0} - \omega) + 2\langle \omega_{K=1} | \sigma_1 t^\pm | 0 \rangle^2 \delta(\omega_{K=1} - \omega)], \quad (5)$$

in $[g_A^2/4\pi]$ units. To obtain this expression, the initial and final states in the laboratory frame have been expressed in terms of the intrinsic states using the Bohr-Mottelson factorization [52].

The specific treatment of odd-A systems was described [31,47] by considering two types of GT contributions. One type is from phonon excitations in which the odd nucleon acts only as a spectator. The transition amplitudes in the intrinsic frame are in this case basically the same as in the even-even case, but with the blocked spectator excluded from the calculation. The other type of transition involves the odd nucleon and is treated perturbatively by taking into account phonon correlations to first order in the quasiparticle transitions. The excitation energies of the GT states with respect to the ground state in the daughter nuclei have been discussed in Ref. [47] for both types of transitions in terms of the QRPA phonon energy and the quasiparticle energies.

The β-decay half-life is obtained by summing all the allowed transition strengths to states in the daughter nucleus with excitation energies lying below the corresponding Q energy, $Q_\beta \equiv Q_{\beta^-} = M(A,Z) - M(A,Z+1) - m_e$, written in terms of the nuclear masses $M(A,Z)$ and the electron mass (m_e), and weighted with the phase space factors $f(Z, Q_\beta - E_{\mathrm{ex}})$,

$$T_{1/2}^{-1} = \frac{(g_A/g_V)_{\mathrm{eff}}^2}{D} \sum_{0<E_{\mathrm{ex}}<Q_\beta} f(Z, Q_\beta - E_{\mathrm{ex}}) B(\mathrm{GT}, E_{\mathrm{ex}}), \quad (6)$$

with $D = 6200$ s and $(g_A/g_V)_{\mathrm{eff}} = 0.77(g_A/g_V)_{\mathrm{free}}$, where 0.77 is a standard quenching factor. The same quenching factor is included in all the figures shown later for the GT strength distributions. The bare results can be recovered by scaling the results in this paper for $B(\mathrm{GT})$ and $T_{1/2}$ with the square of this quenching factor.

The Fermi integral $f(Z, Q_\beta - E_{\mathrm{ex}})$ is computed numerically for each value of the energy including screening and finite size effects, as explained in Ref. [53],

$$f^{\beta^\pm}(Z, W_0) = \int_1^{W_0} pW(W_0 - W)^2 \lambda^\pm(Z, W) dW, \quad (7)$$

with

$$\lambda^\pm(Z,W) = 2(1+\gamma)(2pR)^{-2(1-\gamma)} e^{\mp \pi y} \frac{|\Gamma(\gamma + iy)|^2}{[\Gamma(2\gamma+1)]^2}, \quad (8)$$

where $\gamma = \sqrt{1-(\alpha Z)^2}$; $y = \alpha ZW/p$; α is the fine structure constant and R the nuclear radius. W is the total energy of the β particle, W_0 is the total energy available in $m_e c^2$ units, and $p = \sqrt{W^2 - 1}$ is the momentum in $m_e c$ units.

III. RESULTS AND DISCUSSION

In this section, I present first the PECs in the isotopic chains studied. Quadrupole deformation parameters as well as charge r.m.s. radii (r_c) are analyzed as a function of the mass number. Then, energy distributions of the GT strength corresponding to the local minima in the PECs are calculated. Finally, half-lives are evaluated and compared with the experiment.

A. Structural isotopic evolution

In Fig. 1 the PECs, i.e., the energies relative to that of the ground state, are plotted as a function of the quadrupole deformation β for the neutron-rich Ge, Se, Kr, Sr, Zr, Mo, Ru, and Pd isotopes. The results correspond to the SLy4 interaction. The isotopes covered in this study include middle-shell

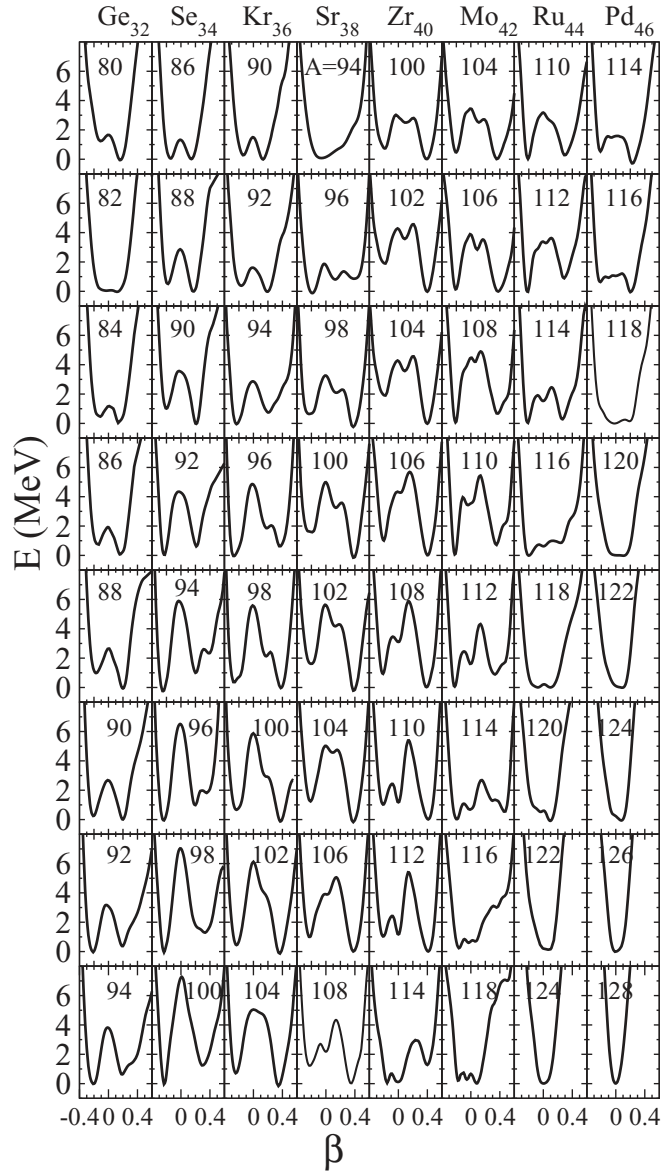

FIG. 1. Potential energy curves for even-even neutron-rich Ge, Se, Kr, Sr, Zr, Mo, Ru, and Pd isotopes obtained from constrained HF + BCS calculations with the Skyrme force SLy4.

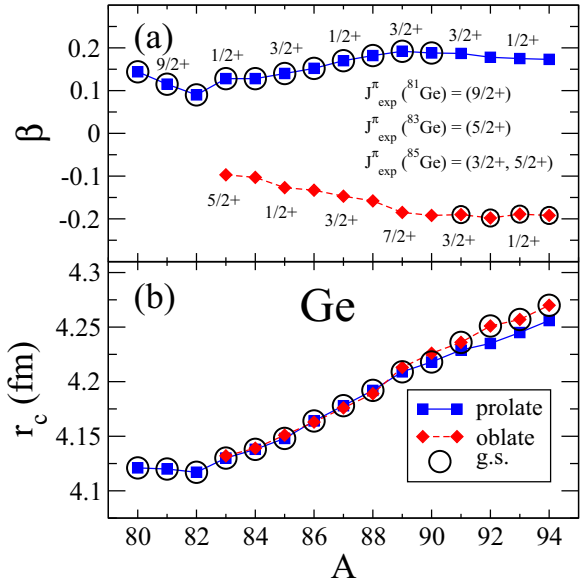

FIG. 2. (Color online) Isotopic evolution of the quadrupole deformation parameter β (a) and charge radius (b) corresponding to the energy minima obtained from the Skyrme interaction SLy4 for Ge isotopes. Ground-state results are encircled.

nuclei with proton numbers between shell closures $Z = 28$ and $Z = 50$, namely $Z = 32,34,36,38,40,42,44,46$ and neutron numbers between shell closures $N = 50$ (as in ^{82}Ge) and $N = 82$ (as in the heaviest ^{128}Pd).

In most of the isotopic chains one can see the appearance of several equilibrium nuclear shapes, whose relative energies change with the number of neutrons. In Ge isotopes, prolate shapes that are ground states in the lighter isotopes are found with the only exception of ^{82}Ge, where a spherical shape is found in accordance with its $N = 50$ semimagic character. At

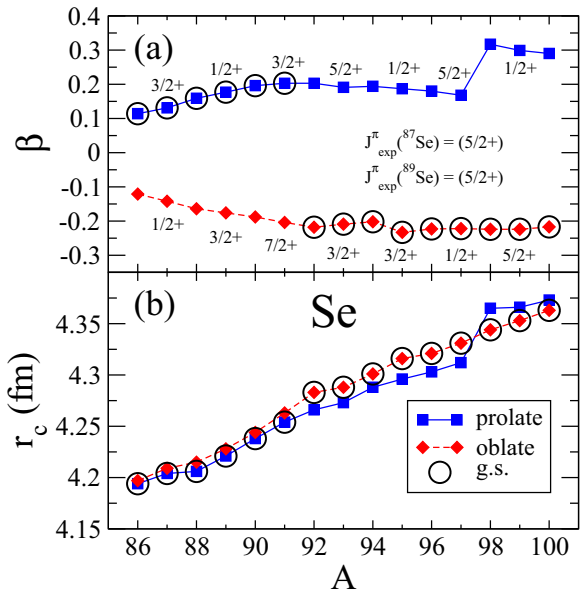

FIG. 3. (Color online) Same as in Fig. 2, but for Se isotopes.

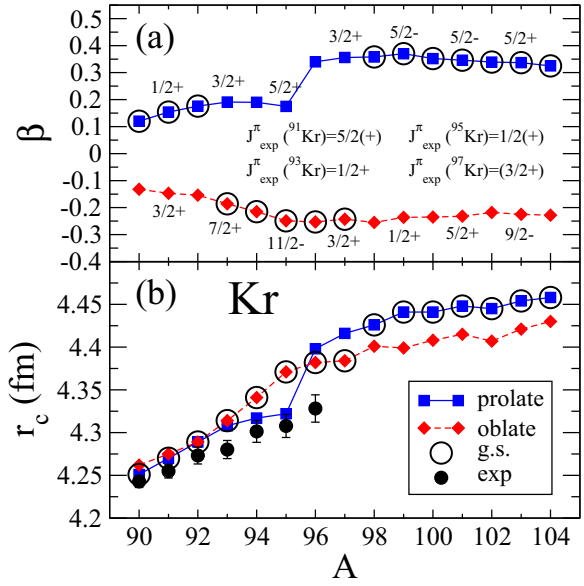

FIG. 4. (Color online) Same as in Fig. 2, but for Kr isotopes. Experimental charge radii are from [59].

$N = 58,60$ (^{90,92}Ge) oblate and prolate shapes are practically degenerate in energy and oblate shapes become ground states for heavier isotopes. The case of Se isotopes is similar with oblate and prolate minima all along the isotopic chain. The lighter (heavier) isotopes have prolate (oblate) ground states with transitional isotopes around $N = 58,60$(^{92,94}Se). In this case the energy barriers are more pronounced than in the case of Ge isotopes. Kr isotopes show competing shapes in the lighter isotopes that become oblate at $N = 58,60$ (^{94,96}Kr) and then turn into prolate shapes beyond ^{98}Kr. In the heavier isotopes, as in the case of Se isotopes, shape coexistence is

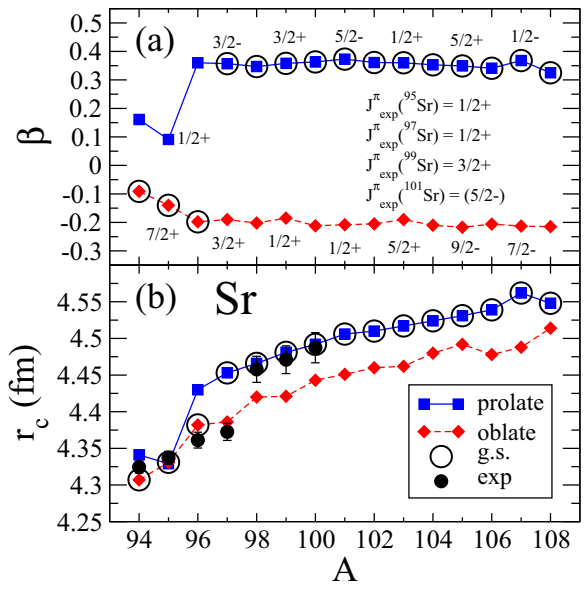

FIG. 5. (Color online) Same as in Fig. 2, but for Sr isotopes. Experimental charge radii are from [59].

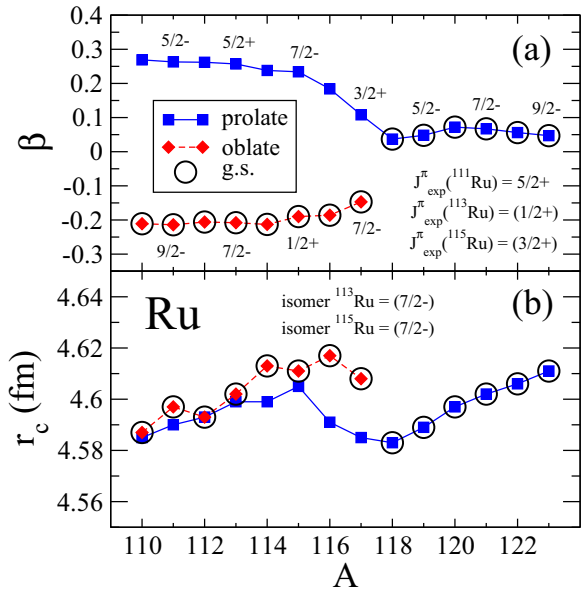

FIG. 6. (Color online) Same as in Fig. 2, but for Ru isotopes.

found with very well-developed oblate and prolate minima separated with high energy barriers. Sr isotopes show a transition from oblate at $N = 58$ (^{96}Sr) to prolate at $N = 60$ (^{98}Sr) with a two minima structure for heavier isotopes. The cases of Zr and Mo isotopes were discussed in Refs. [37,38]. Both oblate and prolate minima are observed in the lighter isotopes of Zr and Mo with prolate ground states. Whereas the prolate shape remains ground state in most of the heavier Zr isotopes, oblate shapes are lower in energy for the heavier Mo isotopes. Finally, Ru and Pd isotopes show oblate and prolate minima in the lighter isotopes and a gradual transition into spherical shapes as one approaches the shell closure at $N = 82$.

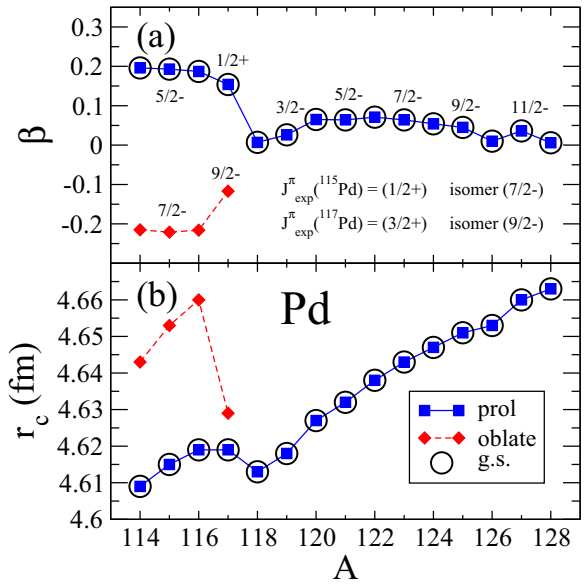

FIG. 7. (Color online) Same as in Fig. 2, but for Pd isotopes.

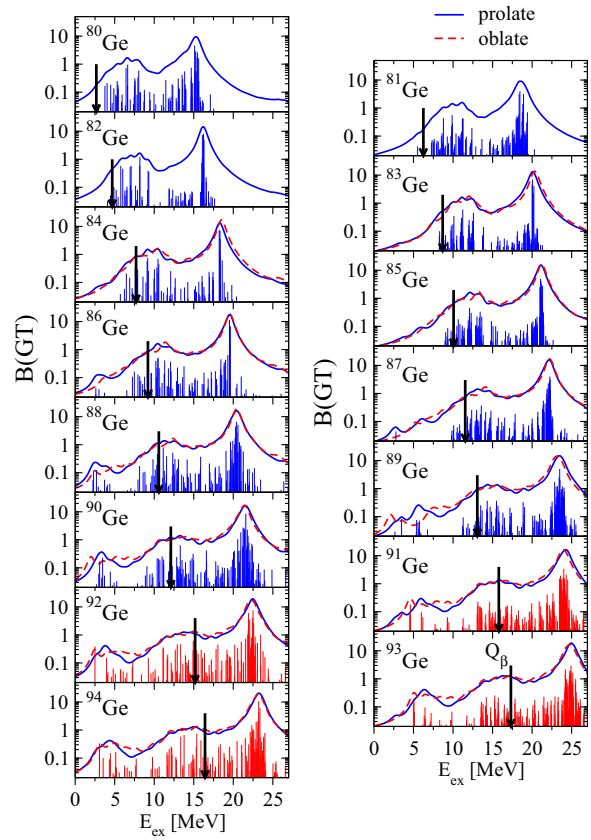

FIG. 8. (Color online) QRPA-SLy4 Gamow-Teller strength distributions for Ge isotopes as a function of the excitation energy in the daughter nucleus. The calculations correspond to the various equilibrium deformations found in the PECs.

In summary, a large diversity of nuclear structures are found in this mass region, from spherical to well-deformed shapes, passing through soft transitional nuclei and even possible shape-coexistence structures. This rich variety of shapes represents a challenge to any theoretical model trying to describe them in a unified manner. In the next subsections the results are compared with the available experimental data, which are restricted at present to β-decay half-lives. Then, the theoretical approach will be tested against this information and the limitations of the model will be established.

These results are in qualitative agreement with similar calculations obtained in this mass region from different theoretical approaches, including macroscopic-microscopic methods based on liquid drop models with shell corrections [54,55], relativistic mean fields [56], as well as nonrelativistic calculations with Skyrme [5] and Gogny [8,9,57] interactions. Thus, a consistent theoretical description emerges, which is supported by the still scarce experimental information available [2,10–16,58].

The isotopic evolution can be better appreciated in Figs. 2–7, where quadrupole deformations β (a) and r.m.s. charge radii r_c (b) of the various energy minima are plotted as a function of the mass number A. The deformation corresponding to the ground state for each isotope is encircled. Also shown in these figures for odd-A isotopes, are the spin

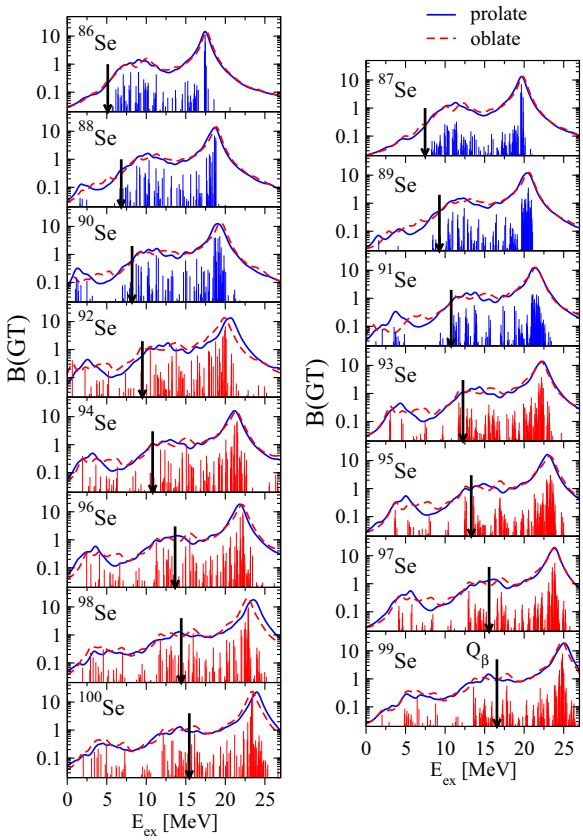

FIG. 9. (Color online) Same as in Fig. 8, but for Se isotopes.

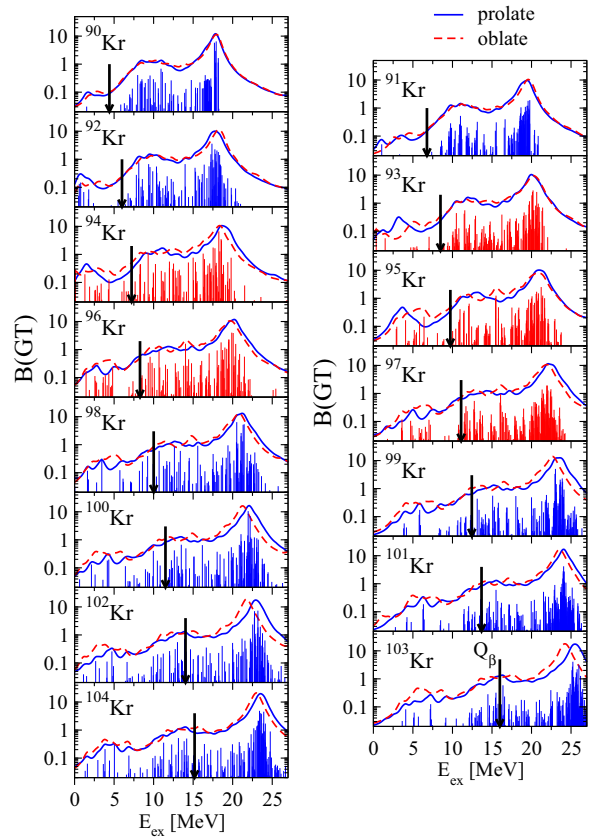

FIG. 10. (Color online) Same as in Fig. 8, but for Kr isotopes.

and parity (J^π) of the different shapes and the experimental assignments [44]. The experimental assignments based on systematics estimated from trends in neighboring nuclides have not been included.

In Fig. 2 for Ge isotopes one can see clearly the shape transition at $A = 90$–92 ($N = 58$–60) from prolate shapes with $\beta \approx 0.2$ to oblate shapes with $\beta \approx -0.2$. Charge r.m.s. radii have not been measured in these isotopes, but it is expected from these calculations a very smooth behavior given that the magnitude of β in the prolate and oblate sectors is very similar. Figure 3 shows the analogous results for Se isotopes. In this case one can see the transition from prolate ($\beta \approx 0.2$) to oblate ($\beta \approx -0.2$) at $A = 92$ ($N = 58$). The prolate shape grows in the heavier isotopes ($\beta \approx 0.3$), but they are never ground states and then, the expected increasing in the charge radii is smooth. Kr isotopes in Fig. 4 show first a shape transition from prolate ($\beta \approx 0.15$) to oblate ($\beta \approx -0.25$) and a subsequent transition from oblate to prolate ($\beta \approx 0.35$) shapes. The radii are sensitive to these transitions, although the measured radii [59] seem to favor prolate shapes in the lighter isotopes. Sr isotopes in Fig. 5 show a clear transition from oblate to strong prolate ($\beta \approx 0.4$) deformations at $A = 96$–98 ($N = 58$–60). This shape transition is well correlated with the trend change observed in the charge radii that shows a sizable jump between ^{96}Sr and ^{98}Sr both theoretical and experimentally [59]. In the case of Ru (Pd) isotopes shown in Fig. 6 (Fig. 7), one can see a smooth transition from deformed oblate (prolate) solutions in the lighter isotopes to spherical shapes in the heavier ones. This change is felt in the trends of the radii, but no experiments with which to compare are yet available.

Spins and parities in odd-A isotopes can be compared with their experimental assignments. In the Ge isotopes the calculations agree reasonably well with the assignments taking into account that oblate and prolate shapes are very close in energy and that a $1/2^+$ isomer is observed experimentally in ^{83}Ge at 248 keV. In the lighter Se isotopes, $1/2^+$ and $3/2^+$ states are obtained, whereas experimental assignments are $(5/2^+)$. In both isotopes, $5/2^+$ states very close in energy to the ground states are also obtained, although somewhat above. Similarly, in the lighter Kr isotopes the experimental assignments are obtained very close in energy to the ground states, although slightly above. On the other hand, a $7/2^+$ isomer is experimentally observed in ^{93}Kr at 355 keV that corresponds to the ground state here. Sr isotopes exhibit a nice agreement. The measured spin and parities of ground states in ^{95,99,101}Sr correspond to the prolate calculations. A $(7/2^+)$ state is also observed experimentally in ^{95}Sr at 56 keV. In ^{97}Sr the observed $1/2^+$ ground state appears as an excited state. It is also worth noting that the prolate ground state $(3/2^-)$ for this isotope is observed experimentally at 645 keV. In the case of Ru isotopes the measured J^π are difficult to reproduce. They are found in the calculations, but not as ground states. On the other hand, the negative parity $7/2^-$ states found in the calculations are also seen experimentally at low energies. In particular, an isomeric state $(7/2^-)$ at an undetermined energy

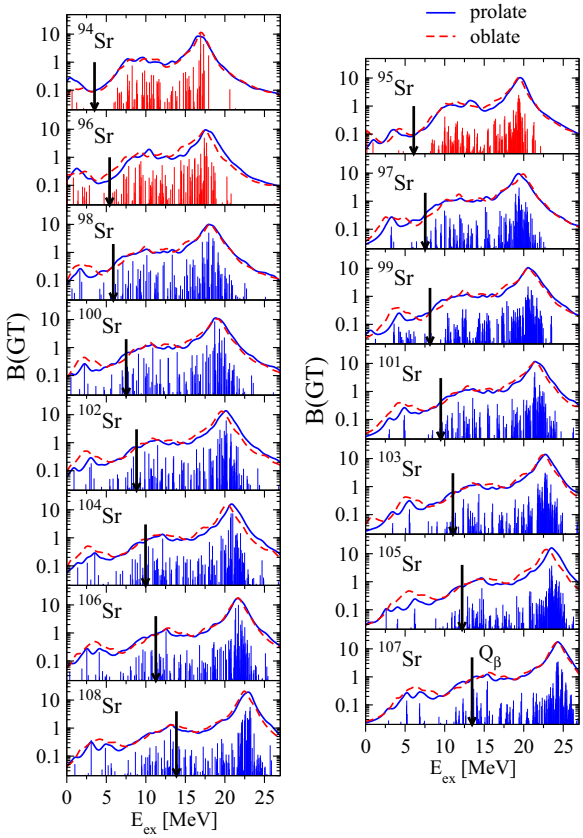

FIG. 11. (Color online) Same as in Fig. 8, but for Sr isotopes.

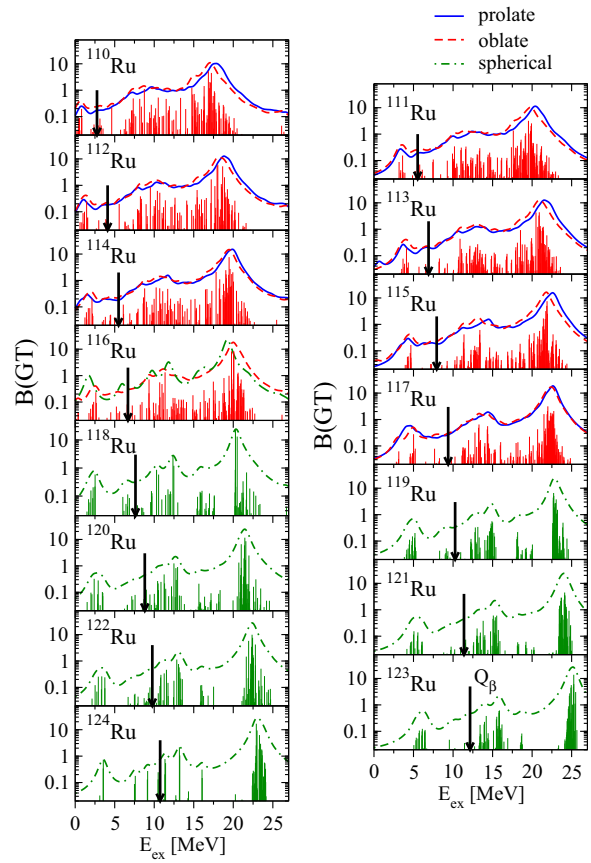

FIG. 12. (Color online) Same as in Fig. 8, but for Ru isotopes.

was seen in ^{113}Ru. Finally, in Pd isotopes the negative parity isomers, which are oblate in this description, are reproduced in the calculations, but not the ground states.

B. Gamow-Teller strength distributions

In the next figures, the energy distributions of the GT strength corresponding to the various deformed equilibrium shapes are shown for each isotopic chain. The results are obtained from QRPA with the force SLy4 with pairing correlations and with residual interactions with the parameters written in Sec. II. The GT strength is plotted versus the excitation energy of the daughter nucleus with a quenching factor 0.77. Zr and Mo isotopes were already studied in Refs. [37,38] and are not repeated here.

Figures 8–13 contain the results for Ge, Se, Kr, Sr, Ru, and Pd isotopes. The energy distributions of the individual GT strengths corresponding to the ground-state shapes are shown, together with continuous distributions for the ground-state shapes as well as for the other possible shapes, obtained by folding the strength with 1-MeV width Breit-Wigner functions. Q_β values are shown with vertical arrows. In both cases, even and odd isotopes, the Q_β values increase with the number of neutrons in each isotopic chain and the values in the odd-A isotopes $(Z,N+1)$ are about 2–3 MeV larger than the values in the neighbor even-even isotopes (Z,N). The general structure of the GT distributions is characterized by the existence of a GT resonance, which is placed at increasing excitation energy as the number of neutrons N increases in a given isotopic chain. The total GT strength also increases with N, as it is expected to fulfill the Ikeda sum rule. The various shapes produce quite similar GT strength distributions on a global scale. Nevertheless, the small differences among the various shapes at the low energy tails (below the Q_β) of the GT strength distributions that can be appreciated because of the logarithmic scale, lead to sizable effects in the β-decay half-lives.

Unfortunately, comparison with experiment is still not possible for the GT strength distributions, the measured half-lives will be compared to the calculations in the next subsection. Comparison with calculated GT distributions from other theoretical approaches is also restricted to the few cases where these results have been published [33,35]. In Refs. [33,60] the authors performed QRPA calculations with deformed Woods-Saxon potentials and realistic CD-Bonn residual forces using the G-matrix formalism and compared these results with the results obtained from separable forces. While in Ref. [33] the comparison between the results obtained from realistic or separable residual interactions is restricted to the half-lives, in Ref. [60] the authors compared those results in the context of two-neutrino double-beta decay, concluding that both approaches, realistic and separable, lead to similar results. On the other hand, in Ref. [35] the Skyrme force SLy4 was used to generate the mean field as it is done in this work. The residual interaction in the ph channel was self-consistently

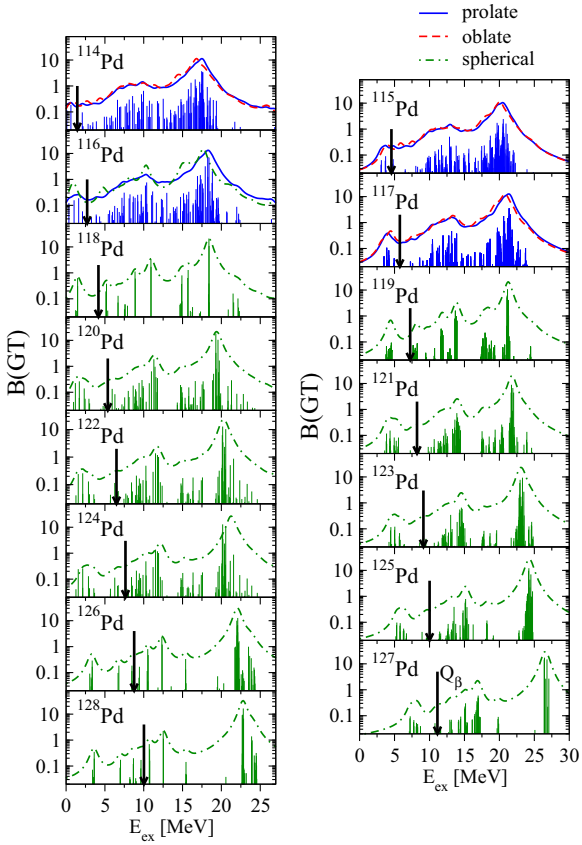

FIG. 13. (Color online) Same as in Fig. 8, but for Pd isotopes.

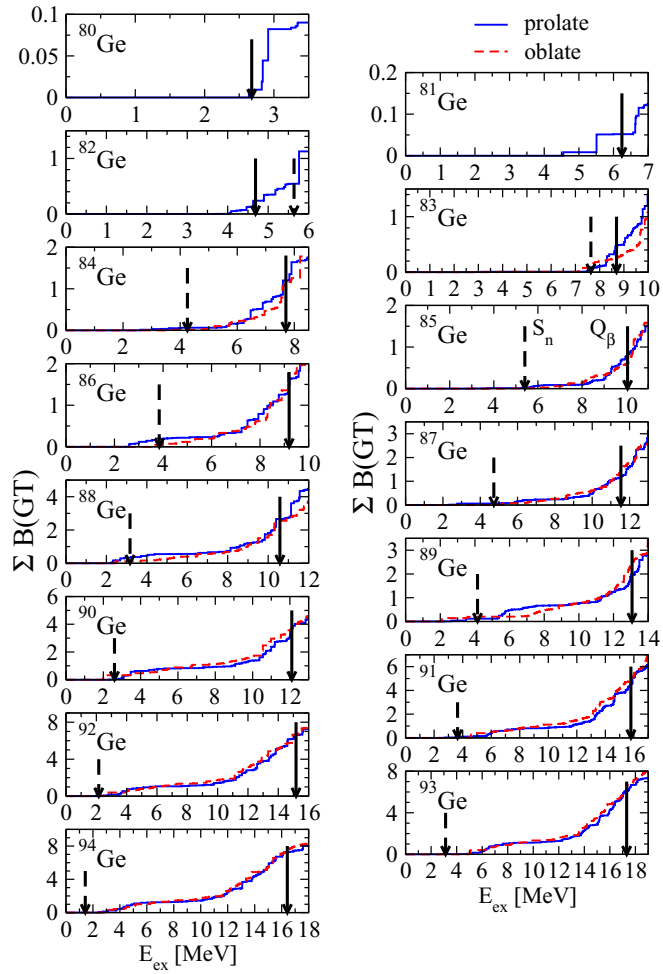

FIG. 14. (Color online) QRPA-SLy4 accumulated GT strengths in Ge isotopes calculated for the various equilibrium shapes. Q_β and S_n energies are shown by solid and dashed vertical arrows, respectively.

introduced and not reduced to a separable form. Finally the pp residual interaction was written as a contact force with a coupling strength fitted to reproduce the half-life in ^{100}Zr. The GT strength distributions in neutron-rich Zr isotopes obtained from this approach were compared with the corresponding distributions obtained with separable forces in Figs. 5 and 6 in Ref. [35]. From this comparison one can conclude that in many aspects the main characteristics of the consistent force are maintained by a separable force with a much lower computational cost. The comparison of the half-lives shows also a remarkable agreement between both approaches.

In the next figures, Figs. 14–19, one can see in more detail the accumulated GT strength in the energy region below the corresponding Q_β energy of each isotope, which is the relevant energy range for the calculation of the half-lives. The vertical solid (dashed) arrows show the Q_β (S_n) energies, taken from experiment [44]. In these figures the sensitivity of these distributions to deformation can be appreciated and one can understand that measurements of the GT strength distribution from β decay can be, in particular cases, an additional source of information about the nuclear deformation, as it was shown in Refs. [49–51]. The GT strength distribution in odd-A isotopes is found to be displaced to higher energies (typically about 2–3 MeV) with respect to the even-even case. The shift corresponds roughly to the breaking of a neutron pair and therefore it amounts to about twice the neutron pairing gap. Below this energy only transitions involving the odd nucleon are possible.

The energy distribution of the GT strength is fundamental to constrain the underlying nuclear structure. For a theoretical model, it represents a more demanding test than just reproducing half-lives or total GT strengths that are integral quantities obtained from these strength distributions properly weighted with phase factors [see Eq. (6)]. These quantities might be reproduced even with wrong strength distributions. This is of special importance in astrophysical scenarios of high densities and temperatures that cannot be reproduced in the laboratory. Given that the phase factors in the stellar medium are different from those in the laboratory, the stellar half-lives become dependent on the electron distribution in the stellar plasma that eventually may block the β-particle emission [61]. Therefore, to describe properly the decay rates under extreme conditions of density and temperature, it is not sufficient to reproduce the half-lives in the laboratory. One needs, in addition, to have a reliable description of the GT strength distributions [62,63].

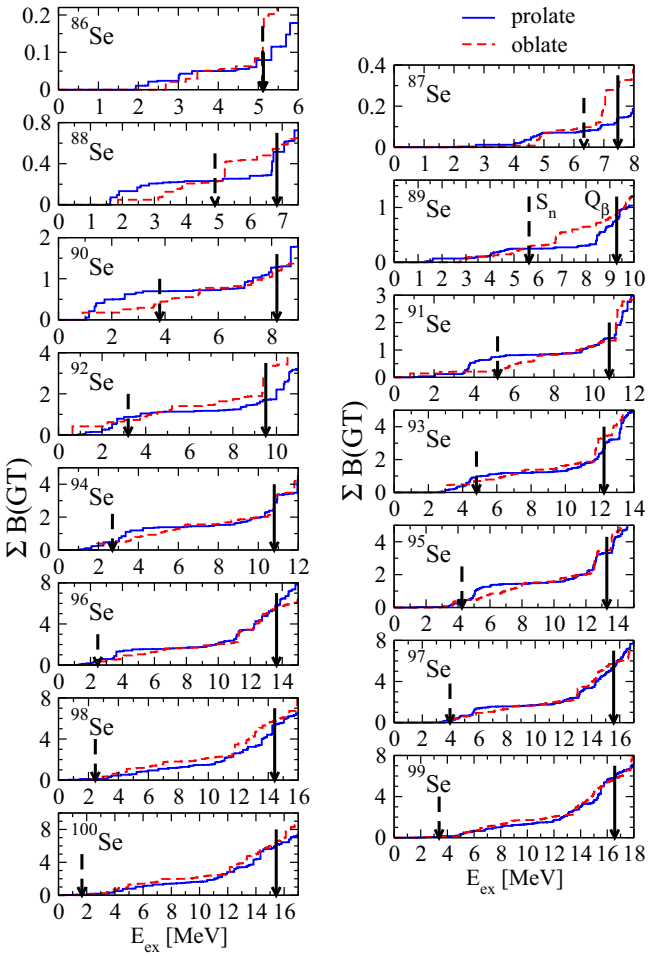

FIG. 15. (Color online) Same as in Fig. 14, but for Se isotopes.

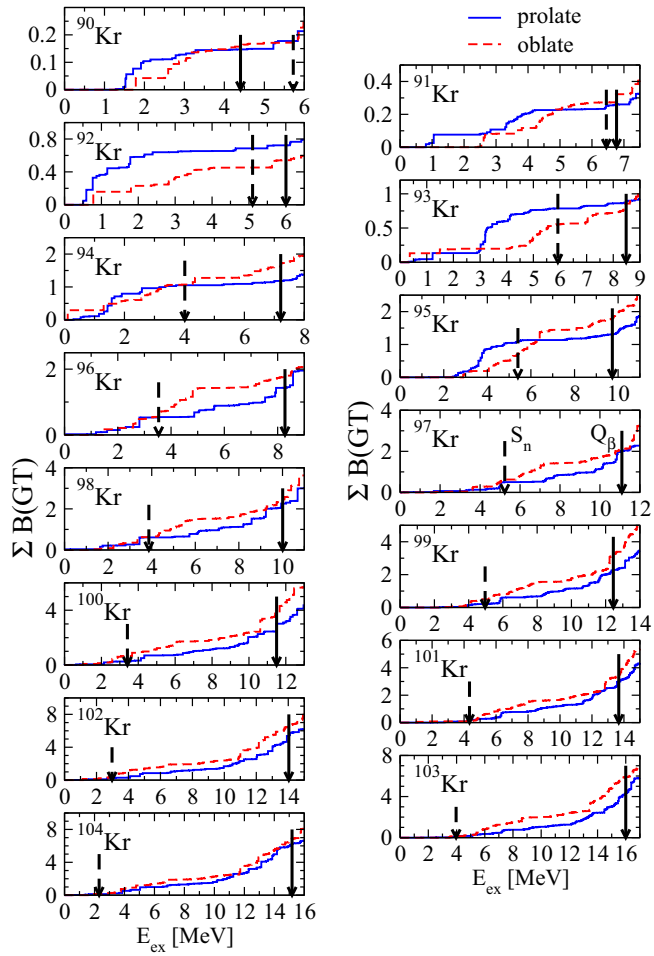

FIG. 16. (Color online) Same as in Fig. 14, but for Kr isotopes.

C. Beta-decay half-lives

The calculation of the half-lives in Eq. (6) involves knowledge of the GT strength distribution and of the β energies (Q_β-E_{ex}), which are evaluated by using Q_β values obtained from the mass differences between parent and daughter nuclei obtained from SLy4 with a zero-range pairing force and Lipkin-Nogami obtained from the code HFBTHO [64].

In Figs. 20–25 the measured β-decay half-lives (solid dots; open dots stand for experimental values from systematics) [23,44] are compared with the theoretical results obtained with the prolate, oblate, and spherical equilibrium shapes, for the various isotopic chains. In Fig. 20 one can see the half-lives for Ge isotopes. The lighter isotopes are not well reproduced, being largely overestimated. This point will be discussed later. The half-lives obtained from oblate shapes are larger than the corresponding prolate ones. This feature is correlated with the GT strength contained below the Q_β energy in Figs. 8 and 14. Prolate shapes, which are closer to experiment, are also the ground states in this range of masses according to the calculations (see Fig. 2). For heavier isotopes, the half-lives for oblate and prolate shapes are very similar. In the case of Se isotopes in Fig. 21, the calculations also overestimate the half-lives of the lighter isotopes, but the agreement with experiment is in this case much better. In the middle region the experimental half-lives, which are taken from systematics, are reasonably well reproduced. The half-lives of heavier isotopes exhibit a somewhat flat behavior. Half-lives of Kr isotopes are shown in Fig. 22. As in the previous figures, the half-lives from the oblate shapes are larger than the prolate ones in the lighter Kr isotopes, but the situation is reversed at ^{94}Kr. This is again nicely correlated with the GT strength at low excitation energies shown in Fig. 16. In general, the half-lives in the middle region are well described. This is also true for Sr and Ru isotopes in Figs. 23 and 24, respectively, where the trends observed experimentally are well reproduced, except for the lighter Sr isotopes that are clearly underestimated and the heavier Ru isotopes, where the data from systematics fall down faster than the calculations. Finally, in the case of Pd isotopes, shown in Fig. 25, the calculations underestimate (overestimate) the measured half-lives in the lighter (heavier) isotopes.

All in all, the agreement with experiment is reasonable, especially in the middle regions. These regions contain in general well-deformed nuclei, where the present approach is more suitable. On the other hand, weakly deformed transitional isotopes, such as light Ge and Se isotopes and heavy Ru and Pd isotopes are not so well described. Furthermore, in the light isotopes of all the isotopic chains, which are closer

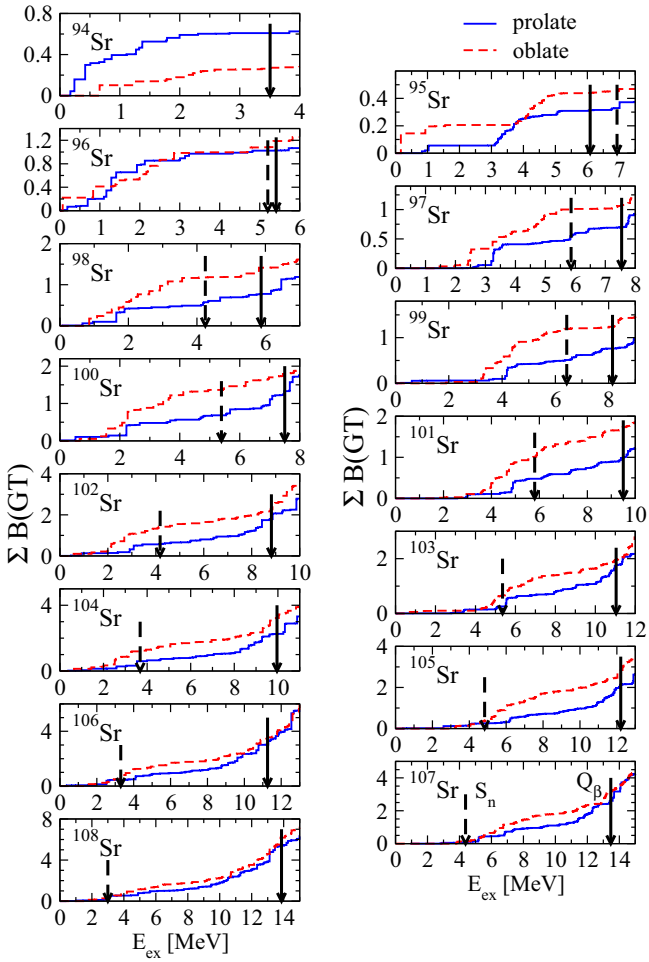

FIG. 17. (Color online) Same as in Fig. 14, but for Sr isotopes.

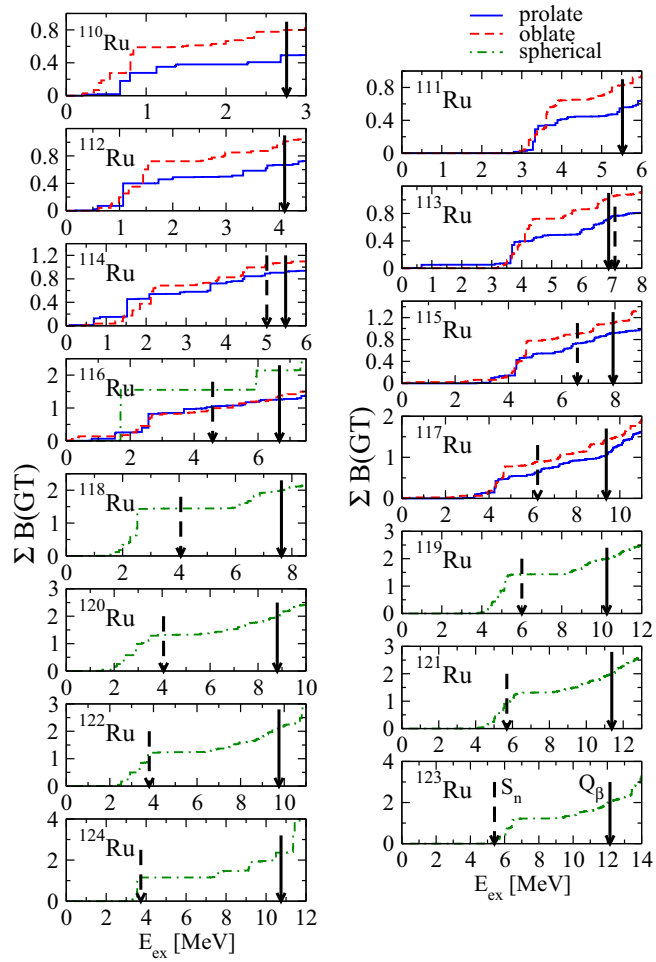

FIG. 18. (Color online) Same as in Fig. 14, but for Ru isotopes.

to the valley of stability, the half-lives are larger because of the small Q_β energies involved. In these cases the half-lives are determined exclusively by the very low energy tail of the GT strength distribution contained in the narrow window below Q_β. Therefore, tiny variations in the description of the GT strength distribution in the low-lying energy region can drive sizable effects in the half-lives. Of course it is also important to describe the half-lives of the long-lived isotopes, but their significance to constrain the GT strength distribution is minor because the half-lives are insensitive to most of this distribution.

Half-lives for neutron-rich Kr, Sr, Zr, and Mo isotopes calculated from self-consistent deformed QRPA calculations with the Gogny D1M interaction and experimental values of Q_β [36] agree with the results in this work within the uncertainties of the calculations. The agreement is also very reasonable between the calculated half-lives and those obtained from deformed QRPA calculations using deformed Woods-Saxon potentials to generate the mean field and complemented with realistic CD-Bonn residual forces [33,34]. The agreement is also good with the results in Ref. [35] using the Skyrme force SLy4 with consistent residual interactions in the ph channel as mentioned earlier. Figure 7 in that reference displays this comparison.

It is also worth noticing that the worst agreement with experiment occurs in the light Ge isotopes, as well as in heavy Pd isotopes. In these cases the calculations overestimate the experiment leaving room for contributions coming from first forbidden (FF) transitions. One can understand from simple qualitative arguments that the role of FF transitions is expected to be more important in lighter Ge and in Pd isotopes. Thus, for $_{32}$Ge, $_{34}$Se, $_{36}$Kr, and $_{38}$Sr isotopes, the last occupied proton orbitals come basically from the $2p_{3/2}$,$1f_{5/2}$, and $2p_{1/2}$ negative-parity spherical shells. On the other hand the neutrons in $^{80-94}$Ge isotopes occupy orbitals belonging to the $1g_{9/2}$,$2d_{5/2}$, and $1g_{7/2}$ positive-parity spherical shells. Therefore, in the β-decay, one neutron in a positive-parity state is transformed into a proton that would sit in a negative-parity state, thus suppressing GT and favoring FF transitions in the low-lying transitions. This is particularly true for the lighter Ge isotopes. In the heavier ones, other neutron states with negative parity ($1h_{11/2}$) have to be considered because of deformation effects. The same argument can be applied to the lighter Se, Kr, and Sr isotopes, but in these cases proton states from positive parity ($1g_{9/2}$) are closer in energy and would participate in the decay favoring GT transitions. The situation is different in the case of Ru and Pd isotopes. Now the available proton states for the decay are of positive parity ($1g_{9/2}$), whereas most of the last

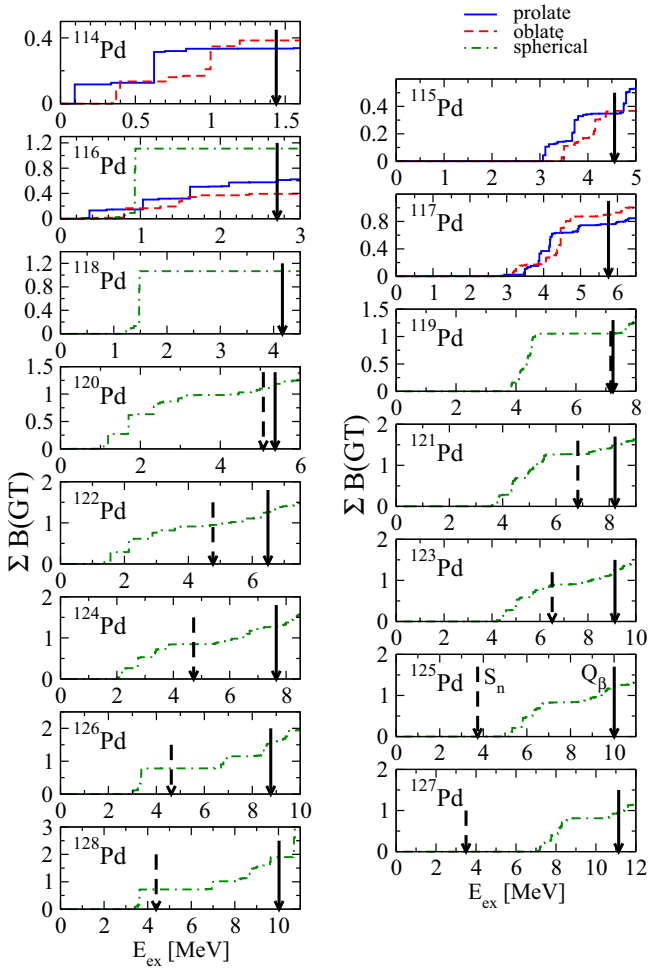

FIG. 19. (Color online) Same as in Fig. 14, but for Pd isotopes.

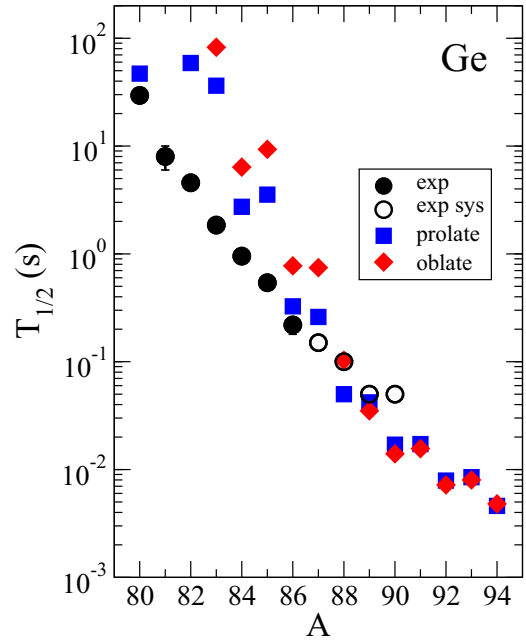

FIG. 20. (Color online) Measured β-decay half-lives for Ge isotopes compared to theoretical QRPA-SLy4 results calculated from different shapes. Circles are experimental values (open circles are experimental values from systematics) [44].

occupied neutrons belong to negative-parity states ($1h_{11/2}$), thus favoring FF transitions. According to calculations [26,33] of the FF transitions in this mass region, minor effects are expected from them. Nevertheless, it would be very interesting in the future to study systematically the FF contributions in all the isotopes in this mass region.

Another feature observed in the present calculations is the existence of some odd-even staggering effect in the calculated half-lives, which is not observed experimentally. This effect is particularly evident in Ru and Pd isotopes. There are not many calculations involving simultaneously even-even and odd-A isotopes, but some of them exhibit some sort of staggering effect as well [33]. The appearance of this effect in the half-lives suggests some deficiency in the model that might be related to the determination of ground-state energies in the odd-A systems [65]. Unfortunately, there are more sources of uncertainty related to the odd-A systems that should be considered as well [66], such as the spin and parity assignments, the blocking procedures or the treatment of the 1-qp excitations involving the odd nucleon. This issue will be the subject of a future investigation in this direction.

It is also interesting to look for the simultaneous appearance of structural effects that eventually can appear in different observables. One example can be seen in the evolution of the experimental half-lives with the number of neutrons in the isotopic chains. At some point one observes discontinuities in the general trends of behavior, such as in the mass regions ^{90,92}Se,^{92,94}Kr, ^{96,98}Sr, and ^{118,120}Ru. These experimental findings on the half-lives are correlated with the

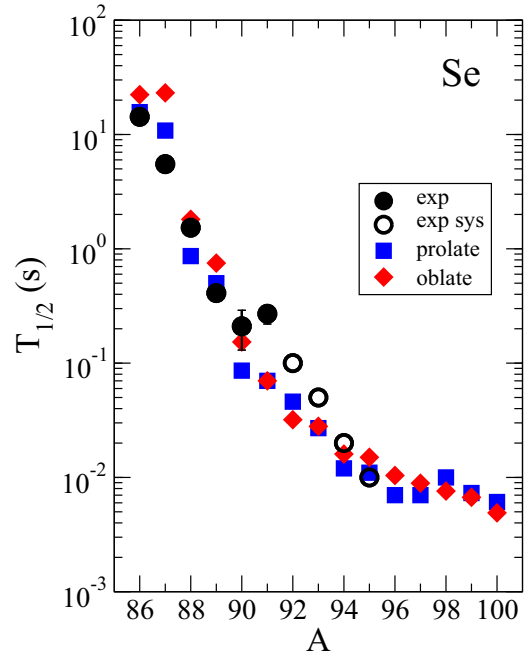

FIG. 21. (Color online) Same as in Fig. 20, but for Se isotopes.

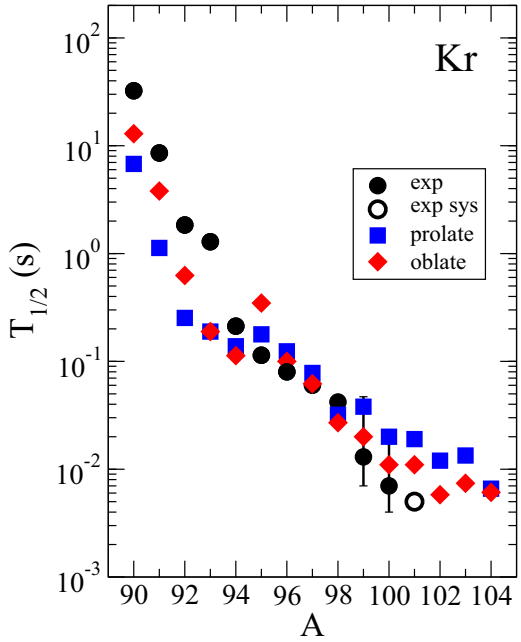

FIG. 22. (Color online) Same as in Fig. 20, but for Kr isotopes. Experimental half-lives are from [23,44].

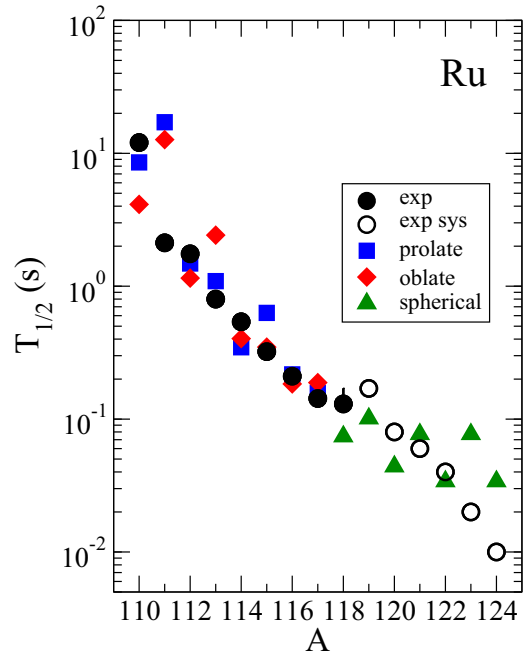

FIG. 24. (Color online) Same as in Fig. 20, but for Ru isotopes.

shape transitions in Figs. 3–6 predicted in the model. One cannot state firmly that these sharp changes in the behavior of the half-lives are signatures of shape transitions, but certainly this correlation cannot be discarded given that a change of the deformation in the nuclear system involves a structural change to whom the half-lives are also sensitive.

Finally, the impact of deformation on the decay properties can be better appreciated in a systematic comparison of the half-lives calculated with both the spherical approximation and the deformation that corresponds to the minimum of the PEC for each isotope. Then, Fig. 26 shows the ratios of the calculated and experimental half-lives for two sets of data corresponding to a spherical calculation (open dots) and to a deformed calculation (solid dots) at the self-consistent deformation that gives the minimum of the PECs. These ratios are plotted as a function of the experimental half-lives (a) and as a function of the quadrupole deformation at the minimum of

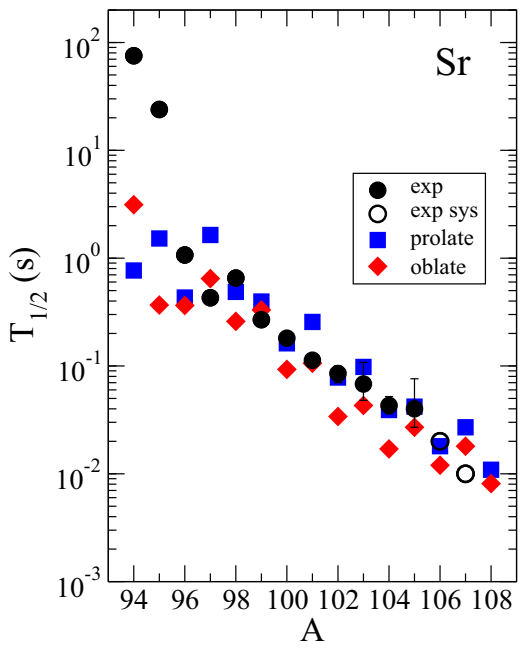

FIG. 23. (Color online) Same as in Fig. 20, but for Sr isotopes. Experimental half-lives are from [23,44].

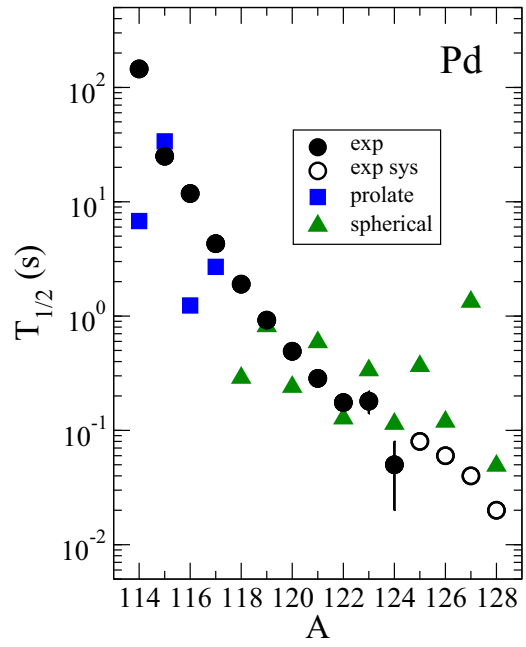

FIG. 25. (Color online) Same as in Fig. 20, but for Pd isotopes.

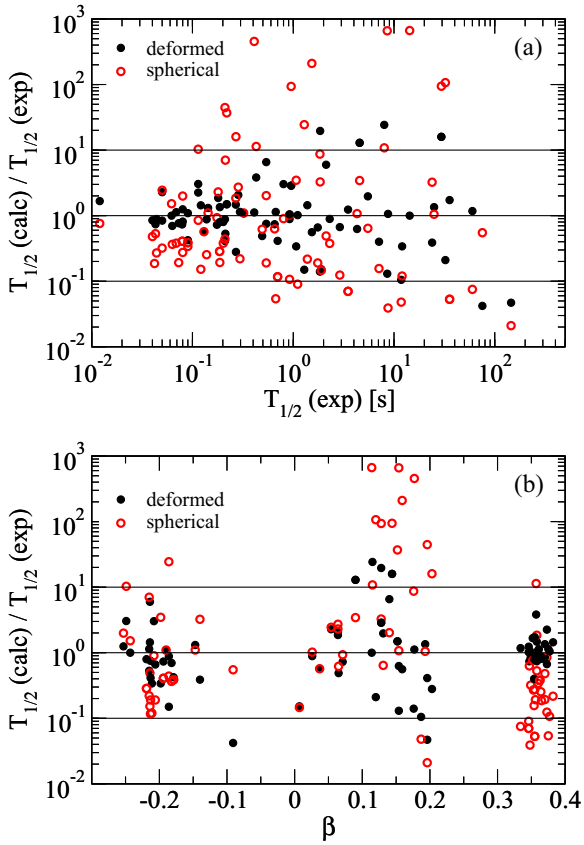

FIG. 26. (Color online) Ratio of calculated to experimental β-decay half-lives for two sets of calculations, with the spherical approximation (open dots) and with the deformation that corresponds to the minimum of the PECs (solid dots). The ratios are plotted as a function of the experimental half-lives (a) and as a function of the quadrupole deformation at the minimum of the PECs (b).

the PECs (b). To increase the size of the sample, in addition to the isotopes considered in this work with measured half-lives, I have also included the set of Zr and Mo neutron-rich isotopes studied in Ref. [38] with measured half-lives. In the upper panel of Fig. 26(a) one can see how deformation improves the description of the half-lives. Practically all the full black dots are contained within the horizontal lines defining the region of one order of magnitude agreement. On the other hand, the results from the spherical calculation are more spread out with larger discrepancy with experiment. One can also see that the results are better in both spherical and deformed calculations for shorter half-lives, whereas the results for larger half-lives show sizable deviations. The latter correspond to isotopes close to the valley of stability with small Q_β values, where the half-lives are only sensitive to the small portion of the GT strength distribution at low excitation energies below Q_β. In the lower panel of Fig. 26(b) one can see the results from a different point of view and it can be studied whether deformation improves the results evenly in the whole range of deformations or whether its effect is stronger at large deformations. Three regions of accumulation of results can be distinguished. Two of them correspond to well-deformed nuclei located at $\beta \approx -0.2$ and $\beta \approx 0.35$. In these regions the deformed calculations clearly improve the results from the spherical ones that show a tendency to underestimate the experiment. The other region corresponds to $0 < \beta < 0.2$ values, where nuclei are softer or transitional and the deformed formalism should be improved. In this region the results are more scattered than in the well-deformed regions, but the deformed calculations show deviations that rarely exceed one order of magnitude, still representing an improvement over the spherical results.

To have a quantitative estimation of the quality of the various calculations, following the analysis made in Ref. [29], the logarithms of the ratios of the calculated and experimental half-lives are introduced through the quantities,

$$r = \log_{10}\left[\frac{T_{1/2}(\text{calc})}{T_{1/2}(\text{exp})}\right]. \tag{9}$$

Then, the average position of the points M_r, the standard deviation σ_r, and the total error Σ_r are defined as

$$M_r = \frac{1}{n}\sum_{i=1}^{n} r_i; \quad \sigma_r = \left[\frac{1}{n}\sum_{i=1}^{n}(r_i - M_r)^2\right]^{1/2}; \quad \Sigma_r = \left[\frac{1}{n}\sum_{i=1}^{n}(r_i)^2\right]^{1/2}, \tag{10}$$

and their corresponding factors $M_r^{10} = 10^{M_r}$, $\sigma_r^{10} = 10^{\sigma_r}$, and $\Sigma_r^{10} = 10^{\Sigma_r}$. The analysis of the results shown in Fig. 26 involving $n = 81$ nuclei leads to the values $M_r^{10} = 1.105$, $\sigma_r^{10} = 10.21$, and $\Sigma_r^{10} = 10.24$ in the spherical case and $M_r^{10} = 0.937$, $\sigma_r^{10} = 3.09$, and $\Sigma_r^{10} = 3.09$ in the deformed one, showing clearly the improvement achieved with the deformed formalism.

IV. CONCLUSIONS

A microscopic approach based on a deformed QRPA calculation on top of a self-consistent mean field obtained with the SLy4 Skyrme interaction was used to study the nuclear structure and the decay properties of even and odd neutron-rich isotopes in the mass region $A \approx 80$–130. The nuclear model and interaction have been successfully tested in the past providing good agreement with the available experimental information on bulk properties all along the nuclear chart. Decay properties in different mass regions have been well reproduced as well. The structural isotopic evolution was studied from their PECs. Depending on the isotopic chain, a large variety of nuclear shapes is found, including spherical shapes, well-developed deformed shapes, and transitional soft shapes. Charge radii have been also investigated, showing the connection between a discontinuous behavior in the isotopic trend with a shape transition and comparing the results with the available measurements from laser spectroscopy. Then, Gamow-Teller strength distributions and β-decay half-lives have been computed for the equilibrium shapes.

The isotopic evolution of the GT strength distributions exhibits some typical features, such as GT resonances increasing in energy and strength as the number of neutrons increases. Effects of deformation are hard to see on a global

scale, but they become apparent in the low excitation energy below Q_β energies, a region that determines the half-lives. Half-lives have been calculated using Q_β energies calculated with the force SLy4. In general, a reasonable agreement with experiment is obtained, especially in the short-lived nuclei of Ge, Se, Kr, Sr, and Ru isotopes. The results are comparable to other calculations using different approaches for the mean field and/or residual interactions. Special difficulties are found to describe properly the half-lives of the lighter Ge isotopes and the Pd isotopes. These are examples of transitional nuclei where the nuclear structure is more involved and the concept of a well-defined shape might not be meaningful.

A systematic comparison of the ratios of the calculated and experimental half-lives was done using both spherical and deformed calculations, showing that the inclusion of deformation improves significantly the description of the decay properties.

Experimental information on the energy distribution of the GT strength is a valuable piece of knowledge about nuclear structure in this mass region. The study of these distributions is within the current experimental capabilities in the case of the lighter isotopes considered in this work. Here, I have presented theoretical predictions for them based on microscopic calculations. Similarly, measuring the half-lives of the heavier isotopes will be highly beneficial to model the *r* process and to constrain theoretical nuclear models. This possibility is also open within present capabilities at RIKEN.

ACKNOWLEDGMENTS

This work was supported by Ministerio de Economía y Competitividad (Spain) under Contract No. FIS2011–23565 and the Consolider-Ingenio 2010 Program CPAN CSD2007-00042.

[1] J. L. Wood, K. Heyde, W. Nazarewicz, M. Huyse, and P. Van Duppen, Phys. Rep. **215**, 101 (1992).
[2] K. Heyde and J. L. Wood, Rev. Mod. Phys. **83**, 1467 (2011).
[3] J. Xiang, Z. P. Li, Z. X. Li, J. M. Yao, and J. Meng, Nucl. Phys. A **873**, 1 (2012).
[4] H. Mei, J. Xiang, J. M. Yao, Z. P. Li, and J. Meng, Phys. Rev. C **85**, 034321 (2012).
[5] P. Bonche, H. Flocard, P.-H. Heenen, S. J. Krieger, and M. S. Weiss, Nucl. Phys. A **443**, 39 (1985).
[6] M. Bender, G. F. Bertsch, and P.-H. Heenen, Phys. Rev. C **78**, 054312 (2008).
[7] M. Bender, K. Bennaceur, T. Duguet, P.-H. Heenen, T. Lesinski, and J. Meyer, Phys. Rev. C **80**, 064302 (2009).
[8] R. Rodriguez-Guzman, P. Sarriguren, L. M. Robledo, and S. Perez-Martin, Phys. Lett. B **691**, 202 (2010).
[9] R. Rodriguez-Guzman, P. Sarriguren, and L. M. Robledo, Phys. Rev. C **82**, 044318 (2010); **82**, 061302(R) (2010); **83**, 044307 (2011).
[10] T. Sumikama *et al.*, Phys. Rev. Lett. **106**, 202501 (2011).
[11] C. Y. Wu *et al.*, Phys. Rev. C **70**, 064312 (2004).
[12] W. Urban *et al.*, Eur. Phys. J. A **22**, 241 (2004).
[13] H. Mach *et al.*, Phys. Lett. B **230**, 21 (1989); H. Mach, M. Moszynski, R. L. Gill, G. Molnár, F. K. Wohn, J. A. Winger, and J. C. Hill, Phys. Rev. C **41**, 350 (1990).
[14] C. Goodin *et al.*, Nucl. Phys. A **787**, 231c (2007).
[15] W. Urban *et al.*, Nucl. Phys. A **689**, 605 (2001).
[16] B. Cheal and K. T. Flanagan, J. Phys. G: Nucl. Part. Phys. **37**, 113101 (2010).
[17] E. M. Burbidge, G. M. Burbidge, W. A. Fowler, and F. Hoyle, Rev. Mod. Phys. **29**, 547 (1959).
[18] J. J. Cowan, F.-K. Thielemann, and J. W. Truran, Phys. Rep. **208**, 267 (1991).
[19] K.-L. Kratz, J.-P. Bitouzet, F.-K. Thielemann, P. Möller, and B. Pfeiffer, Ap. J. **403**, 216 (1993).
[20] N. Nishimura, T. Kajino, G. J. Mathews, S. Nishimura, and T. Suzuki, Phys. Rev. C **85**, 048801 (2012).
[21] http://research.jyu.fi/igisol/JYFLTRAP_masses.
[22] J. Pereira *et al.*, Phys. Rev. C **79**, 035806 (2009).
[23] S. Nishimura *et al.*, Phys. Rev. Lett. **106**, 052502 (2011).
[24] M. Quinn *et al.*, Phys. Rev. C **85**, 035807 (2012).
[25] J. Engel, M. Bender, J. Dobaczewski, W. Nazarewicz, and R. Surman, Phys. Rev. C **60**, 014302 (1999).
[26] I. N. Borzov, J. J. Cuenca-García, K. Langanke, G. Martínez-Pinedo, and F. Montes, Nucl. Phys. A **814**, 159 (2008).
[27] T. Niksic, T. Marketin, D. Vretenar, N. Paar, and P. Ring, Phys. Rev. C **71**, 014308 (2005).
[28] J. Krumlinde and P. Möller, Nucl. Phys. A **417**, 419 (1984).
[29] P. Möller, B. Pfeiffer, and K.-L. Kratz, Phys. Rev. C **67**, 055802 (2003).
[30] H. Homma, E. Bender, M. Hirsch, K. Muto, H. V. Klapdor-Kleingrothaus, and T. Oda, Phys. Rev. C **54**, 2972 (1996).
[31] K. Muto, E. Bender, T. Oda, and H. V. Klapdor-Kleingrothaus, Z. Phys. A **341**, 407 (1992).
[32] F. Frisk, I. Hamamoto, and X. Z. Zhang, Phys. Rev. C **52**, 2468 (1995).
[33] D. L. Fang, B. A. Brown, and T. Suzuki, Phys. Rev. C **88**, 024314 (2013).
[34] D. Ni and Z. Ren, Phys. Rev. C **89**, 064320 (2014); J. Phys. G: Nucl. Part. Phys. **39**, 125105 (2012).
[35] K. Yoshida, Prog. Theor. Exp. Phys. (2013) 113D02.
[36] M. Martini, S. Péru, and S. Goriely, Phys. Rev. C **89**, 044306 (2014).
[37] P. Sarriguren and J. Pereira, Phys. Rev. C **81**, 064314 (2010).
[38] P. Sarriguren, A. Algora, and J. Pereira, Phys. Rev. C **89**, 034311 (2014).
[39] P. Sarriguren, E. Moya de Guerra, A. Escuderos, and A. C. Carrizo, Nucl. Phys. A **635**, 55 (1998).
[40] P. Sarriguren, E. Moya de Guerra, and A. Escuderos, Nucl. Phys. A **691**, 631 (2001).
[41] E. Chabanat, P. Bonche, P. Haensel, J. Meyer, and R. Schaeffer, Nucl. Phys. A **635**, 231 (1998).
[42] M. V. Stoitsov, J. Dobaczewski, W. Nazarewicz, S. Pittel, and D. J. Dean, Phys. Rev. C **68**, 054312 (2003).
[43] D. Vautherin and D. M. Brink, Phys. Rev. C **5**, 626 (1972); D. Vautherin, *ibid.* **7**, 296 (1973).
[44] G. Audi, F. G. Kondev, M. Wang, B. Pfeiffer, X. Sun, J. Blachot, and M. MacCormick, Chinese Phys. C **36**, 1157 (2012);

M. Wang, G. Audi, A. H. Wapstra, F. G. Kondev, M. MacCormick, X. Xu, and B. Pfeiffer, *ibid.* **36**, 1603 (2012).
[45] J.-U. Nabi and H. V. Klapdor-Kleingrothaus, At. Data Nucl. Data Tables **88**, 237 (2004).
[46] P. Sarriguren, E. Moya de Guerra, and A. Escuderos, Nucl. Phys. A **658**, 13 (1999).
[47] P. Sarriguren, E. Moya de Guerra, and A. Escuderos, Phys. Rev. C **64**, 064306 (2001).
[48] P. Sarriguren, R. Alvarez-Rodríguez, and E. Moya de Guerra, Eur. Phys. J. A **24**, 193 (2005).
[49] E. Poirier *et al.*, Phys. Rev. C **69**, 034307 (2004).
[50] E. Nácher *et al.*, Phys. Rev. Lett. **92**, 232501 (2004).
[51] A. B. Pérez-Cerdán *et al.*, Phys. Rev. C **88**, 014324 (2013).
[52] A. Bohr and B. Mottelson, *Nuclear Structure*, Vols. I and II (Benjamin, New York, 1975).
[53] N. B. Gove and M. J. Martin, Nucl. Data Tables **10**, 205 (1971).
[54] J. Skalski, S. Mizutori, and W. Nazarewicz, Nucl. Phys. A **617**, 281 (1997).
[55] P. Möller, J. R. Nix, W. D. Myers, and W. J. Swiatecki, At. Data Nucl. Data Tables **59**, 185 (1995).
[56] G. A. Lalazissis, S. Raman, and P. Ring, At. Data Nucl. Data Tables **71**, 1 (1999).
[57] S. Hilaire and M. Girod, Eur. Phys. J. A **33**, 237 (2007); http://www-phynu.cea.fr/.
[58] M. Albers *et al.*, Phys. Rev. Lett. **108**, 062701 (2012).
[59] I. Angeli, At. Data Nucl. Data Tables **87**, 185 (2004).
[60] D. Fang, A. Faessler, V. Rodin, M. S. Yousef, and F. Simkovic, Phys. Rev. C **81**, 037303 (2010).
[61] K. Langanke and G. Martinez-Pinedo, Nucl. Phys. A **673**, 481 (2000).
[62] P. Sarriguren, Phys. Rev. C **79**, 044315 (2009).
[63] P. Sarriguren, Phys. Lett. B **680**, 438 (2009).
[64] M. V. Stoitsov, J. Dobaczewski, W. Nazarewicz, and P. Ring, Comput. Phys. Commun. **167**, 43 (2005).
[65] T. Duguet, P. Bonche, P.-H. Heenen, and J. Meyer, Phys. Rev. C **65**, 014310 (2001); **65**, 014311 (2001).
[66] N. Schunck, J. Dobaczewski, J. McDonnell, J. Moré, W. Nazarewicz, J. Sarich, and M. V. Stoitsov, Phys. Rev. C **81**, 024316 (2010).